Inorganic Chemistry

pubs.acs.org/IC Article

Alloxazine-Based Ligands and Their Ruthenium Complexes as NADH Oxidation Catalysts and G4 Binders

Maria Jesus Móran Plata, Laura Marretta, Lander Gaztelumendi, German E. Pieslinger, Romina R. Carballo, Elixabete Rezabal, Giampaolo Barone, Virginia Martínez-Martínez, Alessio Terenzi, and Luca Salassa*



Cite This: Inorg. Chem. 2024, 63, 16362-16373



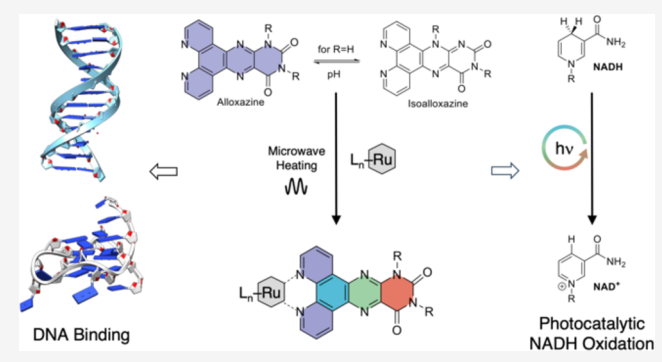
ACCESS

Metrics & More

Article Recommendations

s Supporting Information

ABSTRACT: Flavin-like ligands (L-1 and L-2) with extended π-conjugation were synthesized using microwave-assisted techniques. An N,N-chelating fragment was integrated into alloxazine units, providing binding sites for metal ions while retaining redox activity. The complexation capability of L-1 and L-2 with two prototypical Ru-scaffolds was examined to design Ru(II) complexes (M-1 and M-2), whose electronic properties were studied and compared with their corresponding ligands via absorption and emission spectroscopy, computational analysis (density functional theory (DFT) and time-dependent DFT (TD-DFT)), and cyclic voltammetry (CV). The ability of L-1 and M-1 to undergo alloxazine/isoalloxazine tautomerization was demonstrated to play a crucial role in the photocatalytic oxidation of NADH, including under green and red



wavelengths. Moreover, the interaction of M-1 and M-2 with B-DNA and G-quadruplex structures was investigated. M-2 showed high stabilization of Kit1 and h-Telo oligonucleotides. Meanwhile, M-1 demonstrated switchable emissive properties with B-DNA and induced conformational changes in the h-Telo G-quadruplex structure.

INTRODUCTION

Flavins are ubiquitous cofactors that can carry out single and multielectron redox processes of fundamental relevance in biological systems and chemical technology. Their redox core, composed of the isoalloxazine unit, can accept one or two electrons from various donors and efficiently transfer them to other biological cofactors or substrates.

The interaction between flavins and metal ions has attracted attention, as demonstrated by studies illustrating their incorporation into coordination compounds, resulting in the modulation of electron transfer rates, redox potentials, and excited state reactivities. He expected state reactivities are latively limited, he are their potential as catalysts for their biological functionalities remains largely untapped.

In our recent investigation, we elucidated the utilization of intermolecular interactions between flavins and Pt(IV) complexes to efficiently and selectively photocatalyze the activation of prodrugs into clinically approved Pt(II) chemotherapeutics. This phenomenon extends to flavins integrated into natural or synthetic enzyme scaffolds and loaded onto inorganic nanoparticles and hydrogels. Additionally, we demonstrated that covalently linking a flavin fragment near a Pt(IV) center enhances the reduction and activation of the complex in the dark.

Instead, Bloom and colleagues demonstrated the combination of flavin and Pd catalysis to form C–H and C-X bonds in water, showcasing potential applications in peptide and isotopically enriched peptidomimetic synthesis, as well as in the production of medically relevant small molecules.¹⁵

To advance our research in this area, we opted to combine flavin and metal (photo)reactivities by using extended flavin-like ligands with chelating groups for metal ions. We selected ligands incorporating both a phenanthroline and an alloxazine moiety, which facilitate metal coordination. Alloxazines are structural isomers of natural flavins (isoalloxazines) and differ in the placement of central C=N double bonds and the N(1)/N(10) proton (Figure 1). They exhibit distinct spectroscopic and photophysical properties compared to flavins; however, alloxazines retain redox activity and have recently found application in the development of redox-flow batteries. 16

In this manuscript, ¹⁷ we present the synthesis and reactivity studies of two alloxazine-based ligands and their metal

Received: June 4, 2024 Revised: August 6, 2024 Accepted: August 9, 2024 Published: August 16, 2024





Figure 1. Schematic representation of (a) the isoalloxazine and alloxazine structure and (b) the derivatives studied in this work.

Figure 2. Microwave-assisted (MWAS) synthesis of alloxazine ligands L-1 and L-2, and their Ru(II) complexes M-1 and M-2.

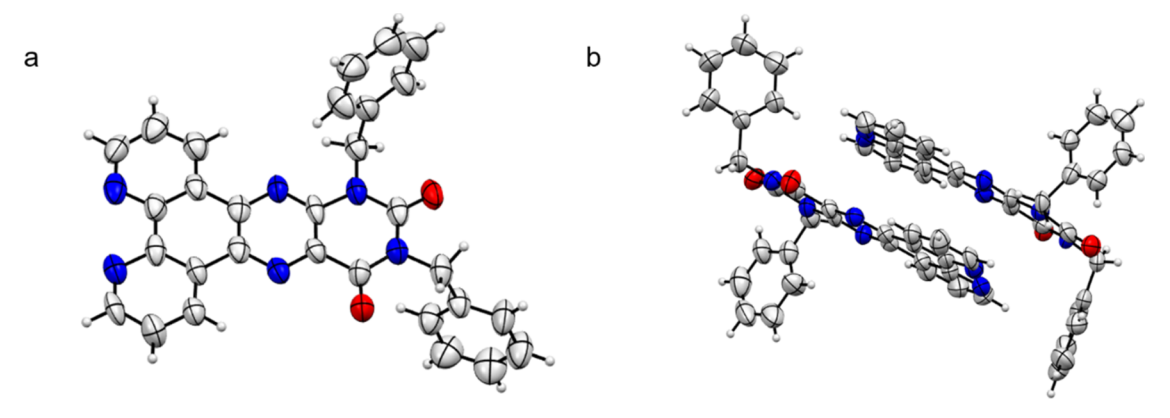
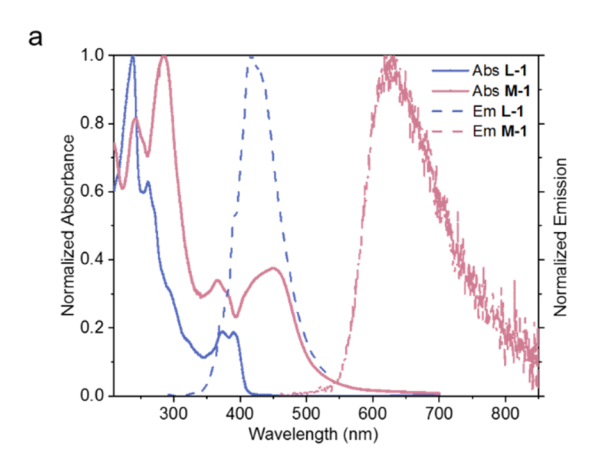


Figure 3. (a) ORTEP diagram and (b) unit cell of L-2. The thermal ellipsoids correspond to a 50% probability.

complexes formed through coordination with prototypical Ru scaffolds (Figure 1). We specifically examine the photophysical properties of these systems, their (photo)tautomerization behavior, and their catalytic activity in the oxidation of NADH. Given their similarity to Ru(II)-dipyridophenazine (dppz) derivatives, renowned DNA intercalators, we also explore the potential of our alloxazine-Ru complexes to bind and stabilize B-DNA and/or G-quadruplex (G4) structures. During the preparation of this manuscript, we discovered that Burgmayer and McGuire had previously reported one of our Ru complexes (vide infra) and investigated its interactions with B-DNA. 19,20 Our study offers novel insights and a deeper comprehension of this class of derivatives.

■ RESULTS AND DISCUSSION

Synthesis and Characterization. The synthetic approach employed in this study to prepare alloxazine ligands and Ru metal complexes is summarized in Figure 2. Alloxazines and dipyridophenazines are typically synthesized through the condensation reaction of 1,10-phenanthroline-5,6-dione with the appropriate diaminopyrimidine, often requiring prolonged reaction times. ^{21,22} Building upon the methodology reported by König and co-workers in 2015, ²³ we achieved the synthesis of the π -system extended heterocycle **L-1** by condensing violuric acid with the corresponding amino phenanthroline precursors. **L-2** was synthesized through the derivatization of



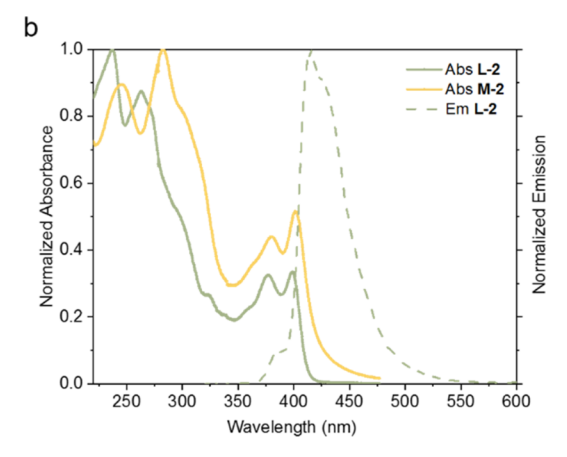


Figure 4. Absorption and emission spectra of (a) L-1 and M-1, and (b) L-2 and M-2 in acetonitrile.

L-1 using benzyl bromide to improve solubility in organic media.²⁴ Microwave-assisted synthesis (MWAS) was employed to expedite reaction times and enhance efficiency, exploiting its known advantages over traditional synthetic methods in both organic and inorganic chemistry domains.²⁵

The subsequent MWAS-complexation process involved the coordination of the phenanthroline motif of L-1 and L-2 with $[Ru(bpy)_2Cl_2]$ and the dichloro(p-cymene)ruthenium(II) dimer, respectively. For the synthesis of $[Ru(bpy)_2(L-1)]$ - $(PF_6)_2$ (M-1), ethylene glycol was selected as the solvent for its high boiling point, which aids in dissolving starting materials. Additionally, it facilitates the maintenance of a reducing atmosphere, essential for stabilizing ruthenium in the +2 oxidation state. The resulting Ru(II) complex, M-1, was insoluble in a cold mixture of ethylene glycol and water (1:1), enabling direct isolation of the pure product. Similarly, [Ru(p-cymene)(L-2)Cl](PF₆) (M-2) was obtained by coordinating L-2 to [Ru(p-cymene)Cl $_2$, with DMF serving as the reaction solvent. Subsequent purification via silica chromatography afforded the desired product.

All synthesized compounds underwent comprehensive characterization, with their structures elucidated through NMR spectroscopy (1 H NMR, 13 C NMR and 1 H $^{-1}$ H COSY) and mass spectrometry. Notably, all compounds were stable in dimethyl sulfoxide (DMSO) solution over 1 week, confirming their chemical robustness (Figures S1 $^{-1}$ S19). Suitable crystals of L-2 were grown by recrystallization in acetonitrile at 4 $^{\circ}$ C (Figure 3). The resolved crystal structure contains two independent molecules in the asymmetric unit stabilized by face-to-face π – π stacking interactions. Structural details are reported in Figure S20 and Table S1. Unfortunately, all our attempts to crystallize the other derivatives were not successful.

Photophysical Studies. We conducted the photophysical characterization of the electronic absorption and emission features of L-1 and L-2, along with the two Ru(II) complexes M-1 and M-2 in acetonitrile, including emission lifetime measurements and quantum yields (Figure 4 and Table 1).

The absorption spectra of L-1 and L-2 exhibit a lowest-energy band with two peaks at 380 and 400 nm, which correspond to $\pi \to \pi^*$ transitions localized prevalently on the pteridine portion of the ligands. Bands at higher energy (<300 nm) demonstrate a more pronounced phenanthroline-centered character (Figure S21). Consistent with previous findings, these assignments also align with TD-DFT calculations conducted on the two ligands and their potential isoalloxazine

Table 1. Summary of Photophysical Parameters for L-1, L-2, M-1 and M-2 in Acetonitrile

	$\lambda_{ m abs}$	ε (10 ⁴ M ⁻¹ cm ⁻¹)	λ_{em} (nm)	φ_{em} (%)	$ au_{ m em}$
L-1	390	0.72	408	7.2	0.75 ns (73%)
	260	3.14			5.21 ns (27%)
L-2	396	0.87	415	6.5	0.75 ns
	379	0.84			
M-1	453	0.91	625	1	170 ns ^a
	382	0.70			
	366	0.80			1.55 μs^{b}
	283	1.88			
M-2	400	1.18	с		
	381	1.14			

^aAerated. ^bDeareated. ^cNot observed.

tautomers at the B3LYP/def2-TZVPP level. Computational predictions performed on both tautomeric forms of the ligands confirm that their electronic structure aligns with the alloxazine type rather than isoalloxazine. This is substantiated by the absence of prominent features in the 400–500 nm region for L-1 and L-2 (Figures S22–S27 and Tables S2–S5).

L-1 and L-2 exhibit a short-lived emission band around 410 nm, characteristic of a singlet $\pi-\pi^*$ state observed previously for dppz derivatives. The fluorescence quantum yields were measured to be 7.2% for L-1 and 6.5% for L-2 (Table 1). The second 5 ns component in the fluorescence decay of L1 may indicate partial tautomerization to the isoalloxazine form, as this lifetime is typical of flavins like FMN. 11

For M-1, the absorption spectrum exhibits features resembling free L-1 in the 250–400 nm range, with a slight blue shift observed in the pteridine band at 375 nm. Based on earlier spectral analyses of related Ru-dppz complexes, ²⁸ the distinctive absorption at 450 nm is attributed to overlapping metal-to-ligand charge transfer (MLCT) transitions between the highest occupied molecular orbital of ruthenium and the lowest unoccupied molecular orbitals of bipyridine (bpy) or L1. Our TD-DFT calculations support this assignment (Figures S28–S30, Tables S6 and S7), also predicting low-probability singlet—singlet transitions at 498 and 529 nm. These findings suggest that excitation of M-1 might be attainable using wavelengths within the green region of the visible spectrum (vide infra).

M-1 emits in the 600–800 nm range with modest efficiency ($\varphi_{\rm em}$ < 1%, $\lambda_{\rm exc}$ = 450 nm). The luminescence is attributed to a 3 MLCT state, as evidenced in Table 1 and Figure S31 by the

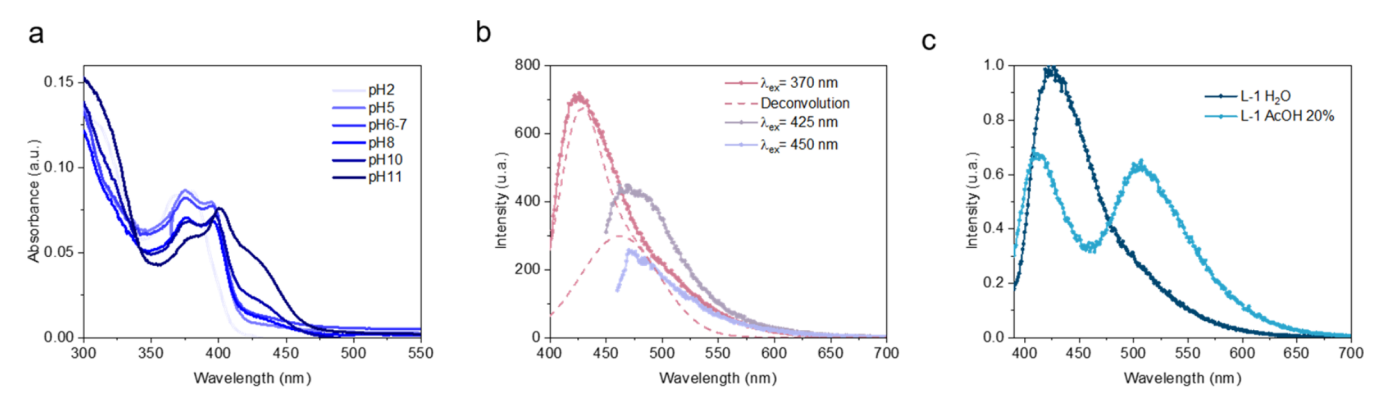


Figure 5. (a) Absorption spectra of L-1 in H_2O (0.5% DMSO) at different pH values; (b) emission spectra of L-1 at pH = 11, λ_{exc} = 370, 425, and 450 nm; and (c) emission spectra of L-1 in H_2O and an AcOH/ H_2O mixture (1:5). AcOH = acetic acid.

characteristic emission lifetime and its increase in deaerated acetonitrile solutions (1.55 μ s) compared to air-equilibrated ones (170 ns). DFT optimization of the lowest-lying triplet state, coupled with the depiction of the spin density surface, substantiated the ³MLCT nature of the emitting state, suggesting its Ru-L-1 origin (Figure S32). Examination of singlet–triplet TD-DFT transitions and their associated electron density difference maps reveals the existence of several other energetically similar ³MLCT states with Ru-L-1 or Ru-bpy nature (Figures S33–S35, Tables S8 and S9). ²⁸

The coordination of L-2 to the *p*-cymene Ru scaffold to form the corresponding complex M-2 minimally impacts the absorption profile of the ligand, leading to a slight red-shift of the main bands. Computational analysis indicates that the lowest-energy absorption band and its shoulder have a mixed MLCT and intraligand charge transfer (ILCT) character (Figures S36–S38, Tables S10 and S11). In acetonitrile, M-2 does not emit light, a result consistent with previous observations. This outcome is typical for pseudo-octahedral piano-stool geometries, as they often suppress ligand emission through the presence of low-lying (triplet) metal-centered states, resulting in derivatives that are either non-emissive or emit weakly.²⁹

Alloxazine derivatives exhibit both ground- and excited-state tautomerization via proton transfer from N(1) to N(10), resulting in photophysical properties akin to those of isoalloxazine in the presence of hydrogen-bonding partners. Lumichrome, a major photodecomposition product of riboflavin, is a prototypical example of this phenomenon. Hence, we investigated whether compounds L-1 and M-1 display isoalloxazine (i.e., flavin-like) characteristics at various pH levels (Figure 5).

UV—vis spectra of L-1 in water (0.5% DMSO) show no significant changes up to pH 11, at which an absorption band at 432 nm emerges, consistent with partial ground-state tautomerization to the isoalloxazine form.³¹ The emission spectra observed at pH 11 reinforce this finding. Upon excitation at 370 nm, emission occurs at 425 nm, corresponding to the (deprotonated) alloxazine form of L1. Deconvolution analysis of this emission reveals a secondary contribution at 470 nm from another species, specifically the isoalloxazine tautomer. When the sample is selectively excited at 425 and 450 nm, enhanced emission at 470 nm is observed, matching the extinction coefficients of the isoalloxazine species at these wavelengths.

Fluorescence experiments conducted in 20% acetic acid/water mixtures, within a pH range where no ground-state

conversion is observed, indicate tautomerization of the ligand in the excited state, as evidenced by the presence of two bands with maxima at 412 and 506 nm, corresponding to the two (protonated) forms of the ligand.³⁰

For compound M-1, no significant changes are observed in the low-energy region of the visible spectra, except for a reduction in the maximum at 390 nm, attributed to N(3) deprotonation. Excited-state tautomerization is not detected as well, since the 3MLCT nature of the emission remains unchanged (Figure S39) in acetic acid/water solutions.

Compounds L-2 and M-2 do not exhibit tautomerization to their isoalloxazine analogs due to benzyl groups at the N1 and N3 positions, which prevents the process. This is confirmed by the lack of substantial changes in pH-dependent absorption spectra for both L-2 and M-2, and the absence of emission at 530 nm in acetic acid/water mixtures for L-2 (Figure S40).

Catalytic NADH Oxidation. To evaluate the catalytic capabilities of the compounds under investigation, we initially investigated their cyclic voltammetry (CV) response in DMSO (Figure S41 and Table S12). For L-1, two one-electron reductions are observed at -1.34 and -1.41 V, with a significant peak separation of 200 mV. While the reduction waves are well resolved, a broad anodic peak suggests slow kinetics and/or potential complications from adsorption phenomena. In the case of compound L-2, the first reduction occurs at -1.38 V and involves a two-electron redox process, followed by a one-electron reduction at a more cathodic potential (-2.10 V), all of which demonstrate considerable reversibility. Upon coordination of L-1 to the [Ru(bpy)₂]²⁺ fragment to form complex M-1, the first ligand reduction shifts to -1.23 V, consistent with the expected stabilization due to the cationic charge of the complex. Furthermore, M-1 exhibits three relatively reversible one-electron reductions. The reductions observed at -1.75 and -1.93 V are bpy-centered, ³² while the process at -2.18 V could represent a second reduction centered over L-1, as previously observed by Olaprath and McGuire for this complex and its dppz analogue.²⁰ CV of M-2 reveals a comparable response pattern to M-1, albeit with anodic shifts in potential (observed at -1.13 and -1.99 V, respectively). Notably, M-2 exhibits an additional redox process at -1.32 V, which is attributed to the reduction of the arene moiety. Consistently, the electrochemical data suggest that both ligands can undergo reduction processes and that the initial reduction event in both M-1 and M-2 is centered on the allox ligand.

Subsequently, we investigated the catalytic capacity of the ligands and their respective metal complexes in the oxidation

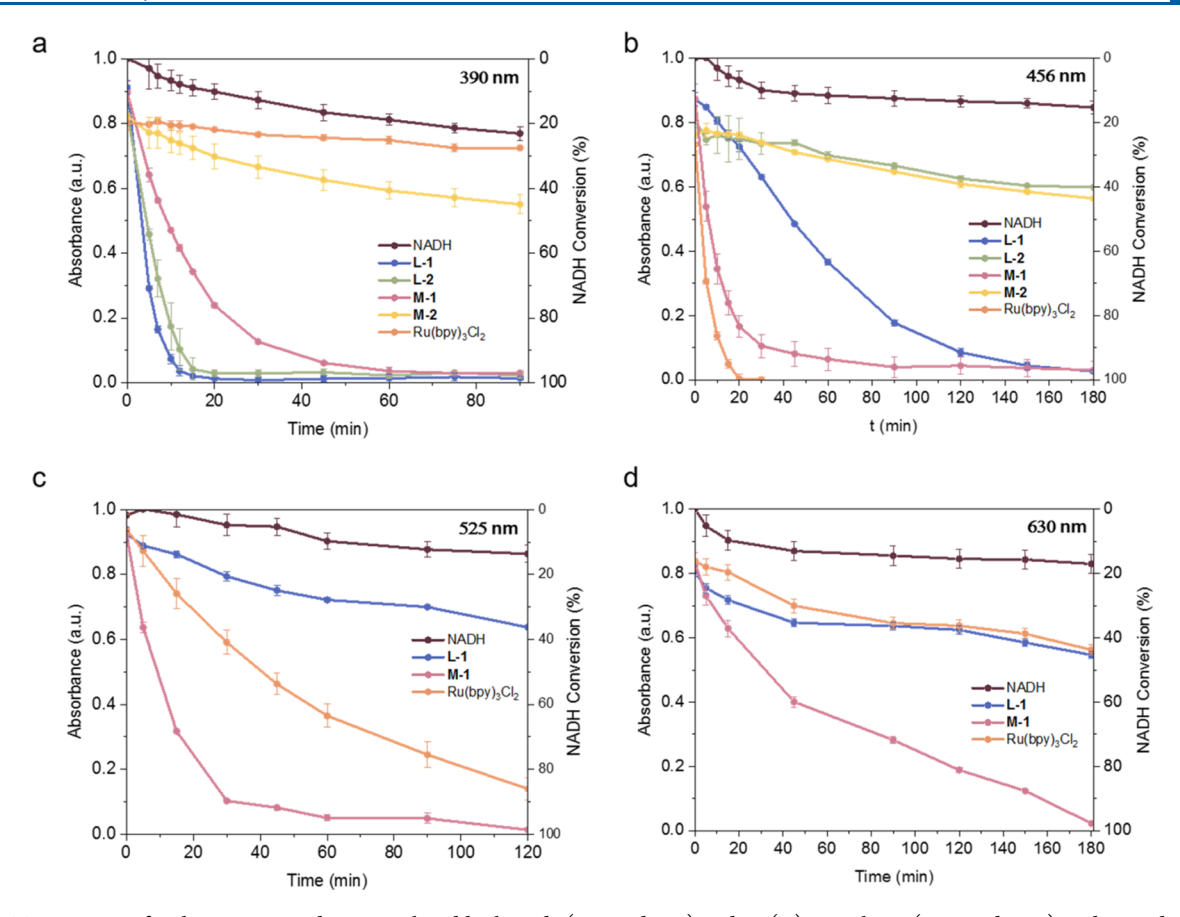


Figure 6. Time courses for the NADH oxidation catalyzed by ligands (L-1 and L-2) and Ru(II) complexes (M-1 and M-2) under irradiation with (a) 390 nm, (b) 456 nm, (c) 525 nm and (d) 630 nm light. [Ru(bpy)₃Cl₂] was also included for comparison purposes. The reactions were performed using 0.4 mM NADH and fixing the substrate/catalyst molar ratio at 10:1.

of NADH, under both dark and light irradiation conditions. This model substrate holds considerable significance due to the increasing importance of enzymatic reactions at the industrial scale, ^{33,34} alongside the pivotal role of catalytic NADH oxidation in biological processes. Besides, the regeneration of electron carriers such as NAD⁺/NADH is crucial for water splitting and hydrogen production. ^{35,36} NADH has also been implicated in the cell-killing mechanism of several catalytic metallodrugs^{37–39} and photodynamic therapy (PDT). Moreover, our recent findings demonstrate that proximity between a flavin unit and a metal center can trigger the activity of Pt anticancer agents in the presence of NADH. ¹⁴

Catalysis experiments utilized 0.4 mM NADH with a fixed substrate/catalyst molar ratio of 10:1. Four excitation wavelengths were applied, and reaction progression was tracked by measuring the reduction in the absorption peak at 340 nm (Figure 6).

In the dark, NADH oxidation rates are slow for all compounds, with M-1 showing higher activity, achieving about 60% conversion after 6 h (Figure S42). Upon 390 nm light irradiation, NADH consumption accelerates significantly for all derivatives except M-2, which exhibits the poorest excited-state features (*vide supra*). L-1 and L-2 fully convert the substrate within 20 min of irradiation, while M-1 requires approximately 1 h. Ru(bpy)₃Cl₂, used as a control, is likely ineffective in NADH oxidation because of the lack of prominent absorption features in this part of the spectrum.

At 456 nm, the photocatalytic activity of the ligands diminishes significantly due to reduced absorption in this

range. Consistently, M-2 remains the least active, while M-1 and Ru(bpy)₃Cl₂ become the most efficient catalyst. It is reasonable to hypothesize that the latter oxidizes NADH through singlet oxygen production. We assessed if this is also true for M-1 by adding an excess of a known singlet oxygen scavenger such as sodium azide (7.5 mM) to the reaction mixture. 40 Under these conditions, the capacity of M-1 to convert NADH to NAD+ remains largely unaffected (Figure S43). ¹H NMR spectra of M-1 in the presence of NADH (1:1) indicate the interaction between the catalyst and the substrate involves the L-1 moiety, as confirmed by the changes in multiple resonances corresponding to M-1 (Figure S44). Based on our previous work⁴¹ and the results reported by Zhang et al., 42 we proposed the catalytic cycle depicted in (Figure S45), involving the transfer of 2 electrons and two protons. NADH likely transfers a hydride to the N5 of the L-1 fragment whereas the ligand N10 extracts a second proton from the aqueous environment.

To evaluate the potential of this complex, catalytic experiments were conducted using a 0.05% loading of M-1, revealing that it could achieve turnover numbers of 1170 within 5 h of blue light irradiation (Figure S46).

Subsequently, green (525 nm) and red (630 nm) light-emitting diodes (LEDs) were utilized to irradiate M-1, aiming to validate the weak absorption features predicted by computational modeling and enabling catalysis at longer excitation wavelengths. Remarkably, at 525 nm, similar photocatalytic activity to that observed at 456 nm was noted. Although somewhat slower conversion rates were observed

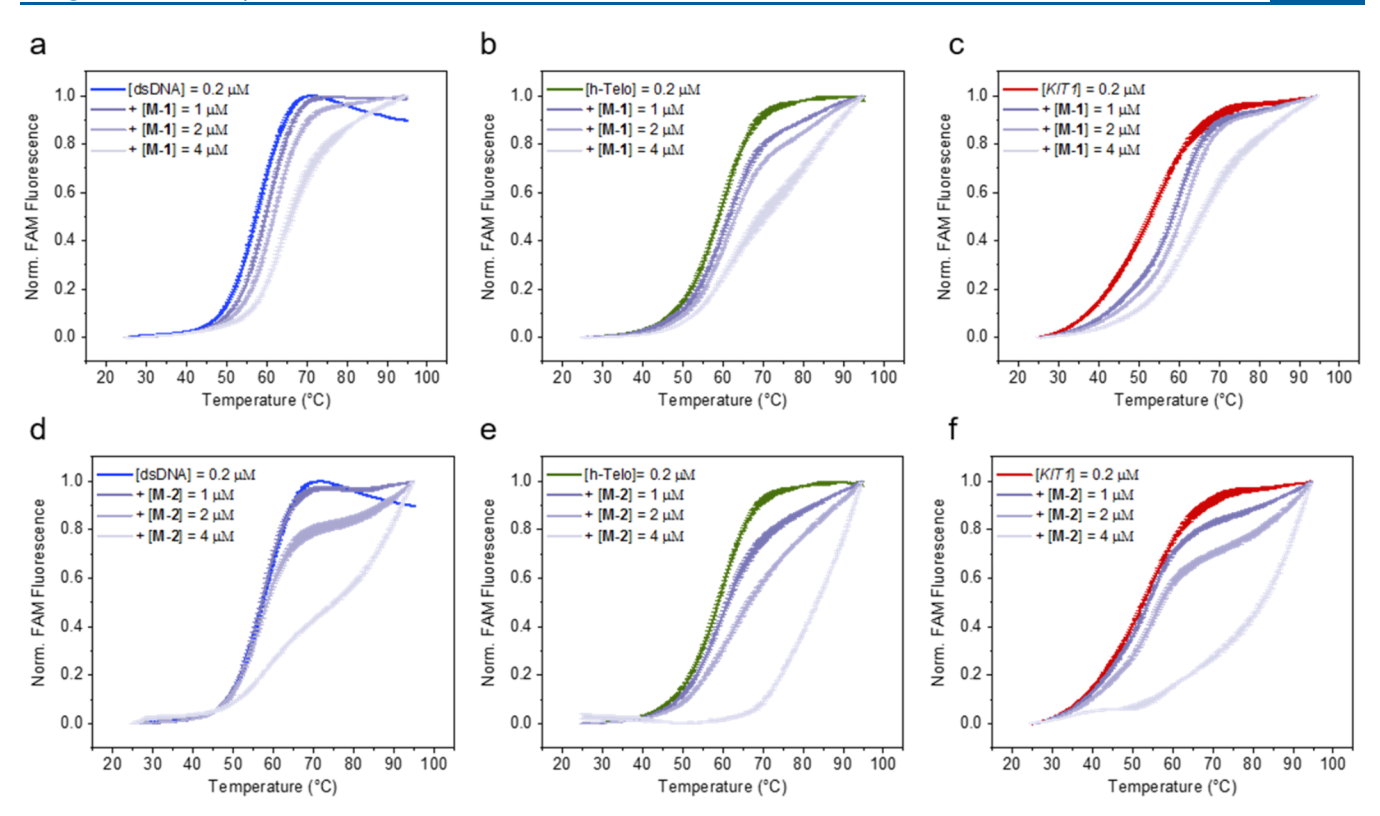


Figure 7. FRET melting profiles of dsDNA, h-Telo and Kit1 upon interaction with (a-c) M-1 and (d-f) M-2 at the indicated concentrations. Buffer: 60 mM potassium cacodylate, pH 7.4.

using the red-emitting LEDs, the results remained noteworthy. In both cases, M-1 outperformed Ru(bpy)₃Cl₂.

Neither ligand absorbs significantly at 456 nm, yet L-1 enhances NADH consumption at this wavelength. Hence, we studied the reaction over time under anaerobic conditions with blue-light irradiation to prevent rapid oxidation of the reduced ligand form by O2 and assess the role of the alloxazineisoalloxazine tautomerism in the catalysis. N₂-purged aqueous solutions containing L-1 and L-2 with NADH (1:10, 400 μ M NADH) underwent irradiation at 456 nm for several minutes, and UV-vis changes were monitored. As shown in Figure S47, before irradiation, both ligands exhibit the typical spectral pattern of an alloxazine (shoulder at 400-425 nm). However, with increasing irradiation time, L-1 displays a bathochromic shift in the low-energy absorption band, attributed to the characteristic absorption spectrum of a doubly reduced isoalloxazine (i.e., flavin hydroquinone). Upon exposure to O2, this species is promptly reoxidized, affording the absorption profile of the alloxazine tautomer of L-1. We confirmed alloxazine-isoalloxazine phototautomerism in the presence of NADH by monitoring the emission of L-1 before and after 1 h of irradiation at 456 nm without O_2 (Figure S48). Under these conditions, L-1 displayed a broad new emission peak at 490 nm, resembling that observed in the presence of acetic acid. Upon exposing the irradiated solution of L-1 to the ambient atmosphere, the spectral features of isoalloxazine vanish, and the emission at 430 nm of the alloxazine isomer is almost entirely restored. This behavior contrasts with that of L-2, which remains unaltered throughout the entire process because of the benzylic substituent at the N(1) position, which prevents isomerization.

DNA-binding Studies. Ruthenium complexes, exhibiting either classic octahedral or piano stool geometries, have long

been recognized for their DNA-binding properties, primarily attributed to the capability of planar ligands to intercalate within the base pairs of DNA molecules. 18 Concerning polypyridyl ligands, 43,44 milestone research conducted by the Barton and Sauvage research groups has revealed that Ru(II) complexes featuring dppz ligands of the type [Ru- $(bpy)_2(dppz)]^{2+}$ and $[Ru(phen)_2(dppz)]^{2+}$ exhibit a high affinity for DNA with luminescence originating from MLCT transitions, whereas the luminescence of the unbound complexes is quenched. This phenomenon, referred to as the DNA "light switch" effect, has garnered considerable attention in the field, and similar Ru(II) complexes have been developed as DNA probes and studied as potential anticancer agents. 45,46 In that regard, Cardin research group reported the crystal structure of a Ru(II) polypyridyl compound containing the dppz ligand in complex with a G4 structure, demonstrating that this class of coordination compounds can also target noncanonical nucleic acid motifs in an enantiospecific manner. 47,48

Therefore, considering the structural similarities between dppz and our ligands L-1 and L-2, we examined the DNA binding properties of compounds M-1 and M-2 using a set of different techniques, including Fluorescence Resonance Energy Transfer melting assay (FRET), circular dichroism (CD) and fluorescence spectroscopy. FRET assay involved incubating M-1 and M-2 at different concentrations with two specific G4 forming oligonucleotides (h-Telo and Kit1) and with dsDNA as a B-DNA model (Table S13). h-Telo and c-Kit1 were chosen because they represent the two most common G4 topologies: hybrid and parallel, respectively. Moreover, h-Telo is a G-rich sequence from the human telomere, and its stabilization by small molecules is known to indirectly inhibit telomerase, an enzyme overexpressed in most cancers. ⁴⁹ In contrast, c-Kit1 is one of three G4-forming sequences located

in the promoter region of the proto-oncogene KIT, which encodes a tyrosine kinase receptor known to be a clinically validated target for treating different tumors. ^{50,51} In this way, we can first assess whether our compounds exhibit a preference for G4s over B-DNA, and also determine if they have an affinity for a specific G4 topology. Ultimately, this will help us evaluate if they can be considered potential anticancer metal-drug candidates.

Initially, we measured the increase in the oligonucleotides melting temperature $(\Delta T_{1/2})$ to assess the ability of the complexes to stabilize these DNA secondary structures. Three [complex]/[oligo] ratios (5:1, 10:1 and 20:1) were examined to investigate a potential concentration effect for both derivatives. Effective stabilization of the oligos was not achieved at the 5:1 ratio; however, we observed an increasing $\Delta T_{1/2}$ depending on the concentration of both M-1 and M-2. The most effective G4 stabilization was obtained with Kit1 and h-Telo, upon interaction with M-2 displaying $\Delta T_{1/2} = 29.7$ and 24.7 °C, respectively, at the 20:1 ratio. The dsDNA showed no stabilization up to the 10:1 ratio, indicating M-2's preference for G4 motifs. Nevertheless, at the highest ratio, the B-DNA model is also stabilized by M-2 (Figure 7 and Table 2). The

Table 2. $\Delta T_{1/2}$ Values of 0.2 μ M dsDNA, h-Telo and Kit1 at the Indicated [Complex]/[Oligo] Ratios with M-1 and M-2^a

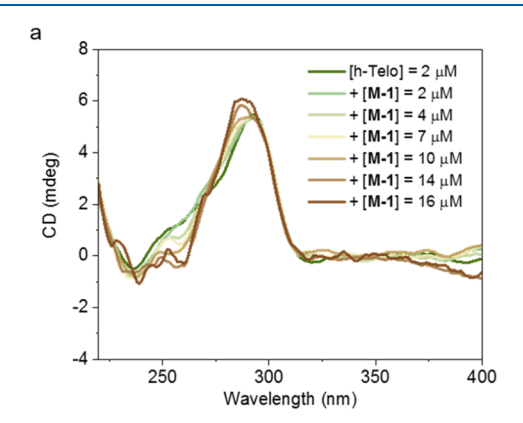
	[complex]/[oligo]	dsDNA	h-Telo	Kit1
M-1	5	2.3	2.6	5.6
	10	4.4	4.2	7.8
	20	8.5	11.0	12.8
M-2	5	0	2.3	1.2
	10	1.0	7.7	4.3
	20	17.9	24.7	29.7

^aThe concentration of DNA is reported in strand. Uncertainty is ≤0.5 for the $\Delta T_{1/2}$ reported.

higher stabilization provided by M-2 compared to M-1 is probably due to the presence of extra aromatic moieties, i.e., the benzyl groups, on the alloxazine ligand which facilitate $\pi - \pi$ stacking interactions with the exposed guanine tetrads. Overall, both metal compounds showed no marked preference for a specific G4 topology, with a slightly higher stabilization of the parallel one.

CD titrations were conducted by incrementally adding both M-1 and M-2 compounds to h-Telo, to investigate potential alterations in the G4 conformation during their interaction. The distinctive CD spectrum of the h-Telo hybrid G4, marked by a prominent positive band centered at 290 nm with a shoulder at 270 nm, undergoes alteration upon interaction with M-1. Notably, an enhancement of the band at 295 nm appears along with a decrease in intensity at 265 nm, indicating a possible conformational shift toward an antiparallel G4 structure (Figure 8a). Interestingly, exposure of h-Telo to M-2, which produces a higher G4 stabilization in the FRET analysis, does not elicit a similar response, with only a comparatively minor decrease observed in the shoulder at 254 nm (Figure 8b). Possibly, the benzyl moieties on M-2 ligand, while helping with $\pi - \pi$ stacking, sterically hamper the direct interaction of the alloxazine core with the G-quadruplex tetrads. A similar G4 conformational shift was reported for a square planar metal complex without bulky substituents, synthesized by some of

Considering the documented switch-ON effect demonstrated by Ru-dppz complexes upon interaction with DNA, we investigated the emission properties of M-1 and M-2 in the presence of both B-DNA and G4 structures. We conducted titration experiments by systematically adding h-Telo or Calf Thymus DNA (CT-DNA, selected as B-DNA model) to the compounds, revealing a distinct behavior. M-2 displays no enhancement in emission in the presence of either DNA structure (data not shown), consistent with its subpar photophysical properties. Conversely, M-1 displays increased emission upon binding with both DNA forms (Figure 9). Binding constants determined for h-Telo and CT-DNA are $9.52 \pm 0.04 \times 10^{3}$ and $3.33 \pm 0.03 \times 10^{4}$, respectively, indicating a comparable affinity toward CT-DNA and h-Telo in these experimental conditions. In a prior study, Dalton et al. 19 described that M-1 shows switch-ON properties reporting a binding constant of 7.2×10^5 in phosphate-buffered saline (PBS). Ru-dppz derivatives exhibit enhanced emission upon DNA binding due to the shielding of phenazine nitrogens from water. Several studies indicate that hydrogen bonding between the ligand and water molecules leads to the population of an intermediate dppz-centered $n-\pi^*$ state, which is repulsive to water molecules and eventually evolves into a dark (nonemissive) $\pi - \pi^*$ dppz state.⁵³ A similar scenario can be hypothesized for M-1.



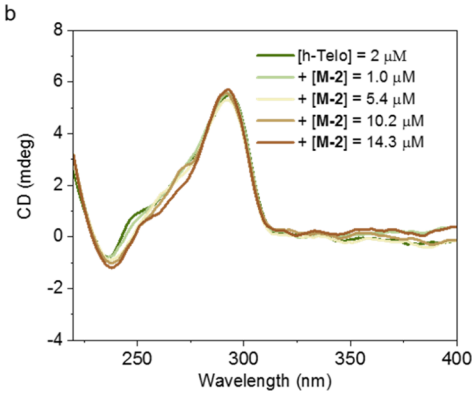


Figure 8. CD spectra of h-Telo in the presence of increasing aliquots of (a) M-1 and (b) M-2 at the indicated concentrations. Buffer: 50 mM Tris-HCl (100 mM KCl), pH = 7.4. The concentration of DNA is reported in strand.

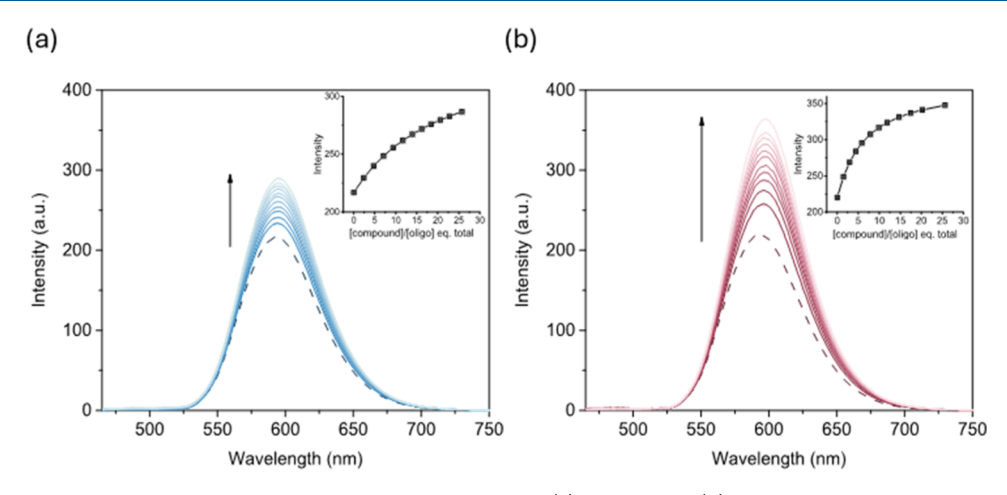


Figure 9. Emission spectra of M-1 in the presence of increasing aliquots of (a) h-Telo and (b) CT-DNA in 50 mM Tris-HCl buffer (100 mM KCl). The arrows indicate the change upon DNA addition. The graphs in the upper right corner illustrate the variation in emission intensity at 593 nm. [M-1] = 5.1μ M.

CONCLUSIONS

We have devised a novel and practical method for the synthesis of alloxazine-based ligands and their coordination compounds utilizing microwave-assisted techniques. These derivatives are emissive, undergo tautomerization, and possess redox activity, attributes encouraging their application in photocatalysis. This study underscores the efficacy of photoirradiation in the catalytic oxidation of NADH, even utilizing green and red wavelengths.

The expanded aromatic moieties of ligands L-1 and L-2 endow their ruthenium complexes with the capability to interact with B-DNA and notably, with G4 structures. M-2 prefers G4 structures, thereby strongly stabilizing Kit1 and h-Telo oligonucleotides. Conversely, the distinct ruthenium scaffold of M-1 assumes differing roles, imparting switchable emissive properties with B-DNA and h-Telo G4, as well as the capacity to induce conformational changes in the h-Telo G4 structure.

EXPERIMENTAL SECTION

Materials and Methods. All reagents employed in this study were of commercial grade and sourced from newly unsealed containers. Milli-Q water underwent purification using a Milipore Direct-Q 3 UV apparatus. Flash chromatography utilized Fisher 60A (70–200 mesh) silica gel, while thin layer chromatography employed Merck 60 F254 foils.

Microwave Reactor. All reactions were conducted under microwave irradiation using the Anton Paar Monowave 400 system, employing 10 or 30 mL microwave vessels.

Nuclear Magnetic Resonance (NMR). ¹H and ¹³C nuclear magnetic resonance (NMR) spectra of the various samples were recorded on a Fourier TM Bruker 300 MHz NMR using standard pulse programs. Chemical shifts were expressed in parts-per-million $(\delta, \text{ ppm})$ and referenced to the residual solvent peaks: deuterated dimethyl sulfoxide (DMSO- d_6) ($\delta H = 2.54$, $\delta C = 39.5$), deuterated chloroform (CDCl₃) ($\delta H = 7.26$, $\delta C = 77.16$), and deuterated acetonitrile (ACN- d_3) ($\delta H = 1.94$, $\delta C = 118.26$).

Mass Spectrometry-Ultrahigh Performance Liquid Chromatography (MS-UPLC). The analysis consisted in a chromatographic separation in an ultrahigh performance liquid chromatography (UPLC, Acquity system from Waters Cromatografia S.A.) coupled to a high-resolution mass spectrometer (Synapt G2 from Waters Cromatografia S.A., time-of-flight analyzer, TOF) by an electrospray ionization source in positive mode (ESI+).

The chromatographic separation was achieved using an Acquity UPLC BEH C18 column (1.7 μ m, 2.1 × 50 mm i.d.) with an Acquity UPLC BEH C18 1.7 μ m VanGuard precolumn (2.1 × 5 mm) (Waters Cromatografia S.A.) and a binary A/B gradient (solvent A: water with 0.1% formic acid and solvent B: methanol). The gradient program was established as follows: initial conditions were 5% B, raised to 100% B over 2.5 min, held at 100% B until 4 min, decreased to 5% B over the next 0.1 min, and held at 5% B until 5 min for reequilibration of the system prior to the next injection. A flow rate of 0.25 mL/min was used, the column temperature was 30 °C, the autosampler temperature 4 °C and the injection volume 2 μ L.

High-resolution mass data were acquired in SCAN mode, using a mass range 100–2000 u in resolution mode (fwhm $\approx 20,000$) and a scan time of 0.1 s. The source temperature was set to 120 °C and the desolvation temperature to 350 °C. The capillary voltage was 0.7 kV and the cone voltage 15 V. Nitrogen was used as the desolvation and cone gas at flow rates of 600 and 10 L/h, respectively. Before analysis, the mass spectrometer was calibrated with a sodium formate solution. A leucine-enkephalin solution was used for the lock mass correction, monitoring the ions at mass-to-charge ratio (m/z) 556.2771 and 278.1141. All of the acquired spectra were automatically corrected during acquisition based on the lock mass. Samples were dissolved in methanol at a concentration of 1 mg/mL and diluted at 20 $\mu \rm g/mL$ for the analysis.

UV-vis Spectroscopy (UV-vis). UV-Vis measurements of the various samples were recorded on a Jasco V-730 spectrophotometer in the range of 200–800 nm, using quartz cuvettes (1 cm pathway length). The samples were solubilized and analyzed at room temperature after proper dilutions in $\rm H_2O$ (5% DMSO) or acetonitrile (ACN).

Emission Spectroscopy. Steady-state fluorescence measurements were carried out in an Edinburgh Instruments Spectrofluorimeter (FLSP920 model), equipped with a xenon flash lamp (450 W) as the excitation source and a photomultichannel tube, PMT (Hamamatsu R2658P) as a detector. The fluorescence spectra were corrected from the wavelength dependence on the detector sensibility. Fluorescence quantum yields were determined via absolute method, through an integrating sphere in the same spectrofluorimeter. Radiative decay curves for ligands L-1 and L-2 were recorded in the same spectrofluorometer with a time-correlated single-photon counting technique using a microchannel plate detector (Hamamatsu C4878) with picosecond time resolution (≈100 ps).

The luminescence lifetime of the triplet state of M-1 was recorded in a transient absorption LP 980 Spectrometer (Edinburgh Instruments) in Laser-Induced Fluorescence (LIF) mode, at 450 nm excitation and 4 mJ power with a Nd:YAG laser coupled to an OPO system from LOTIS (TII 2134) operating at 1 Hz and with a pulse width of 7 ns as excitation. The kinetic decay curves were registered at

625 nm in a PMT detector (Hamamatsu R928) in the presence (aerated solutions) and absence of oxygen (deaerated solution) after bubbling air and nitrogen, respectively, for 10 min.

The fluorescence lifetimes $(\tau_{\rm em})$ were obtained by the FAST (Fluorescence Analysis Software Technology) software (Edinburgh Instruments, Livingston, U.K.) after deconvolution of the instrumental response function in the case of shorter lifetimes (L-1 and L-2) and by a tail fit for longer lifetimes (M-1). The goodness of the exponential fit was controlled by statistical parameters (chi-square, χ^2 values between 0.9 and 1.3 and analysis of the residuals). When necessary, the decay curves were adjusted to a sum of exponential decays using the equation: $I_{\rm fl}(t) = \sum A_{\rm i} {\rm e}^{(t/\tau_{\rm i})}$, where $A_{\rm i}$ is the preexponential term, and $\tau_{\rm i}$ is the fluorescence lifetime.

Emission spectra of M-1 in the presence of DNA samples were recorded with a PerkinElmer LS-50B Luminescence Spectrometer.

Density Functional Theory Calculations. Density functional theory (DFT) computations were employed to fully optimize L-1, L-2, M-1 and M-2 in acetonitrile. Additionally, optimized geometry of the singlet ground state of M-1 was used as the starting point for the optimization of its lowest-lying triplet state species. The calculations were performed with the *Gaussian16* package, ³⁴ at the B3LYP level of theory with the semiempirical dispersion correction of Grimme with Becke-Johnson damping,⁵⁵ using restricted and unrestricted approximations of the Kohn–Sham equations,⁵⁶ depending on the system multiplicity. Previous work on related compounds showed that this functional provided a good description of the structural and electronic features of Ru-based polypyridyl complexes. ^{57,58} All atoms were described with the def2-TZVPP basis set, ⁵⁹ which includes the associated Stuttgart effective-core potentials ⁶⁰ for Ru. Solvation effects were accounted for using the most recent implementation of the implicit IEF-PCM solvation model.⁶¹⁻⁶³ We used tight convergence criteria in the geometry optimizations and default settings for IR calculations. All optimized structures were confirmed as minima by analyzing the harmonic vibrational frequencies. 64 Vertical electronic excitation energies and intensities were evaluated using the time-dependent DFT (TD-DFT)^{65,66} approach with the *Gaussian16* package,⁵⁴ without symmetry constraints. GaussSum 2.2.6⁶⁷ was used to perform spectral simulation, extract spectral data and molecular orbital information, and obtain the electron density difference maps (EDDM). The graphical visualizations were generated by Gauss View 5.0.8,68 i.e., the isovalues were drawn at 0.004 (EDDM) or 0.04 (Kohn-Sham MOs).

Electrochemistry. Cyclic voltammetry (CV) measurements were performed in a three-electrode electrochemical cell equipped with a glassy carbon (\emptyset = 5 mm) working electrode, a platinum sheet as a counter electrode and a silver wire as pseudoreference electrode. The CV measurements were performed using an Autolab PGSTAT 204 potentiostat/galvanostat. [TBA]PF $_6$ (0.1 M) was used as the supporting electrolyte in dry dimethyl sulfoxide and ferrocene (Fc) was used as internal reference. The scan rate was 100 mV/s and the electrolyte was purged with high purity argon before each measurement to remove any traces of oxygen.

Catalytic NADH Oxidation. All catalytic experiments were carried out in air at 298 K. Light irradiation experiments were performed employing LEDs of different wavelengths ($\lambda_{\rm exc}$ = 390, 456, 525, and 630 nm) and optical density of approximately 0.1 mW cm $^{-2}$. NADH consumption with and without light irradiation was determined for both the ligands (L-1, L-2) and Ru-complexes (M-1, M-2). NADH absorption was measured in a microplate reader BioTek Synergy H1. The UV detector wavelength was set at 340 nm. Total run time varied from minutes to hours, depending on the experiment.

60 μ L of 1 mM NADH stock solution in distilled H₂O were added into the wells of a plate to reach a final concentration of 400 μ M in all the experiments. Afterward, the catalyst solution was introduced to initiate the reaction, achieving a final concentration of 40 μ M. This resulted in a NADH/catalyst ratio of 10:1. Milli-Q H₂O was used to complete 150 μ L total volume in all the well-plates. All experiments were performed in triplicates and all data are expressed as the mean \pm standard deviation. Control experiments included NADH alone

without catalyst (400 μ M). The absorption values of all four compounds (40 μ M) at 340 nm was subtracted in all experiments in order to obtain a more accurate comparison of the different systems.

FRET Melting Assay. FRET experiments were performed using a 96-well format Applied Biosystems QuantStudio 6 PCR cycler equipped with a FAM (6-carboxyfluorescein) filter. Oligonucleotide stock solutions, incorporating FAM and TAMRA (6-carboxytetramethylrhodamine) probes, were diluted to the desired concentration in 60 mM potassium cacodylate buffer (pH 7.4). Next, the oligonucleotides were folded into their B-DNA or G4 topology by heating the solutions to 95 $^{\circ}$ C for 5 min, then slowly cooling to room temperature overnight. The final concentration of the oligonucleotides was set at 0.2 μ M (total volume of 30 μ L in each well). Metal complexes were dissolved in DMSO to create a 2 mM stock solution and further diluted with the buffer, ensuring a total percentage of DMSO never exceeded 0.3%. Data were collected in duplicate, in the range of 25–95 °C (with a ramp of 1 °C every 30 s). For comparative analysis across different data sets, emission data were normalized from 0 to 1. $T_{1/2}$ represents the temperature at which normalized FAM emission is 0.5.

Circular Dichroism. CD spectra were obtained using a Jasco J-715 spectropolarimeter at 25 °C by incrementally introducing aliquots of metal complex solution into a constant concentration of DNA solution. Complex stock solutions were prepared in acetonitrile. The experimental parameters were configured as follows: range 400–220 nm; response time 0.5 s; accumulation 4; and speed° 200 nm/min. Titrations were conducted in a Tris-KCl buffer (50 mM Tris-HCl, 100 mM KCl, pH 7.4). The folding of G4 structures was achieved as described in the FRET paragraph.

DNA Binding Studies by Emission Spectroscopy. The titrations were performed using a JASCO FP-8300 spectrofluorimeter. The acquisitions were obtained by setting the parameters: excitation bandwidth 5 nm, emission bandwidth 10 nm, response 0.1 s, medium sensitivity, scan speed 1000 nm/min. The spectra were acquired in quartz cuvettes with an optical path length of 1 cm. Compound stock solutions were prepared in acetonitrile and then diluted in Tris-KCl buffer (50 mM Tris-HCl, 100 mM KCl, pH 7.4). Increasing amounts of DNA in buffer were then added to the solution, waiting approximately 30 s after each addition. Emission intensity was corrected taking account of dilution of the compound. Binding constants were calculated using the Thordarson equation considering all the wavelengths within the range 550–650 nm. 69

X-ray Crystallography. X-ray data collection of suitable single crystals of compounds **L-2** was performed on a SuperNova Single source at offset/far Eos diffractometer. The crystal was kept at 170.00(10) K during data collection. Using Olex2, ⁷⁰ the structure was solved with the ShelXT⁷¹ structure solution program using Intrinsic Phasing and refined with the ShelXL⁷² refinement package using Least Squares minimization. Details of the structure determination and refinement of compounds are summarized in Table S1.

ASSOCIATED CONTENT

Supporting Information

The Supporting Information is available free of charge at https://pubs.acs.org/doi/10.1021/acs.inorgchem.4c02314.

Synthesis and structural characterization; photophysical characterization; DFT and TD-DFT calculations; catalysis experiments, oligonucleotide sequences (PDF)

Accession Codes

CCDC 2358415 contains the supplementary crystallographic data for this paper. These data can be obtained free of charge via www.ccdc.cam.ac.uk/data_request/cif, or by emailing data_request@ccdc.cam.ac.uk, or by contacting The Cambridge Crystallographic Data Centre, 12 Union Road, Cambridge CB2 1EZ, UK; fax: +44 1223 336033.

AUTHOR INFORMATION

Corresponding Author

Luca Salassa — Donostia International Physics Center,
Donostia 20018, Spain; Polimero eta Material Aurreratuak:
Fisika, Kimika eta Teknologia, Kimika Fakultatea, Euskal
Herriko Unibertsitatea UPV/EHU, Donostia 20018, Spain;
Ikerbasque, Basque Foundation for Science, Bilbao 48011,
Spain; orcid.org/0000-0002-2112-9095;
Email: lucasalassa@gmail.com

Authors

Maria Jesus Móran Plata — Donostia International Physics Center, Donostia 20018, Spain; Polimero eta Material Aurreratuak: Fisika, Kimika eta Teknologia, Kimika Fakultatea, Euskal Herriko Unibertsitatea UPV/EHU, Donostia 20018, Spain

Laura Marretta – Dipartimento di Scienze e Tecnologie Biologiche, Chimiche e Farmaceutiche, University of Palermo, Palermo 90128, Italy

Lander Gaztelumendi — Donostia International Physics Center, Donostia 20018, Spain; Polimero eta Material Aurreratuak: Fisika, Kimika eta Teknologia, Kimika Fakultatea, Euskal Herriko Unibertsitatea UPV/EHU, Donostia 20018, Spain

German E. Pieslinger — Donostia International Physics Center, Donostia 20018, Spain; CONICET—Universidad de Buenos Aires, Instituto de Química y Fisicoquímica Biológicas (IQUIFIB), Buenos Aires 1113, Argentina; orcid.org/0000-0003-1334-5211

Romina R. Carballo – CONICET—Universidad de Buenos Aires, Instituto de Química y Fisicoquímica Biológicas (IQUIFIB), Buenos Aires 1113, Argentina

Elixabete Rezabal — Donostia International Physics Center, Donostia 20018, Spain; Polimero eta Material Aurreratuak: Fisika, Kimika eta Teknologia, Kimika Fakultatea, Euskal Herriko Unibertsitatea UPV/EHU, Donostia 20018, Spain; orcid.org/0000-0003-0397-6140

Giampaolo Barone — Dipartimento di Scienze e Tecnologie Biologiche, Chimiche e Farmaceutiche, University of Palermo, Palermo 90128, Italy; orcid.org/0000-0001-8773-2359

Virginia Martínez-Martínez – Departamento de Química Física, Universidad del País Vasco, UPV/EHU, Bilbao 48080, Spain; orcid.org/0000-0001-7551-3714

Alessio Terenzi — Dipartimento di Scienze e Tecnologie Biologiche, Chimiche e Farmaceutiche, University of Palermo, Palermo 90128, Italy; orcid.org/0000-0001-9751-1373

Complete contact information is available at: https://pubs.acs.org/10.1021/acs.inorgchem.4c02314

Notes

The authors declare no competing financial interest.

ACKNOWLEDGMENTS

The authors thank the Spanish State Research Agency (Grants PID2022-139267OB-I00 and PID2020-114347RB-C32), the Gipuzkoa Foru Aldundia (Programa Red guipuzcoana de Ciencia, Tecnología e Innovación 2023; Grant 2023-CIEN-000047-01), the Eusko Jaurlaritza (Grant IT1639-22, IT1584-22 and Elakartek KK-2023/00003) and the UPV/EHU (EHU-G23/03, TransCat Seed) for funding. DIPC is supported by the "Severo Ochoa" Programme for Centres of Excellence in R&D (MINECO, CEX2018-000867-S). SGIKER (UPV/

EHU/ERDF, EU) is acknowledged for technical and human support. R.R.C. and G.E.P. are members of the research staff of CONICET. G.E.P. gratefully thanks CONICET for the CIC scholarship.

REFERENCES

- (1) Flavins and Flavoproteins; Weber, S.; Schleicher, E., Eds.; Springer: Berlin, 2014.
- (2) Rehpenn, A.; Walter, A.; Storch, G.; et al. Molecular Editing of Flavins for Catalysis. *Synthesis* **2021**, *53* (15), 2583–2593.
- (3) König, B.; Kümmel, S.; Cibulka, R. 4. Flavin Photocatalysis. In *Chemical Photocatalysis*; König, B., Ed.; De Gruyter: Berlin, Boston, 2013; pp 45–66.
- (4) Kaim, W.; Schwederski, B. Non-Innocent Ligands in Bioinorganic Chemistry—An Overview. *Coord. Chem. Rev.* **2010**, 254 (13), 1580–1588.
- (5) Fukuzumi, S.; Ohkubo, K. Metal Ion-Coupled and Decoupled Electron Transfer. *Coord. Chem. Rev.* **2010**, 254 (3), 372–385.
- (6) Fukuzumi, S.; Kojima, T. Control of Redox Reactivity of Flavin and Pterin Coenzymes by Metal Ion Coordination and Hydrogen Bonding. *JBIC, J. Biol. Inorg. Chem.* **2008**, *13* (3), 321–333.
- (7) Das, A.; Jobelius, H.; Schleinitz, J.; Gamboa-Ramirez, S.; Creste, G.; Kervern, G.; Raya, J.; Le Breton, N.; Guénet, A.; Boubegtiten-Fezoua, Z.; et al. A Hybrid Bioinspired Catechol-Alloxazine Triangular Nickel Complex Stabilizing Protons and Electrons. *Inorg. Chem. Front.* **2021**, *8* (24), 5286–5298.
- (8) Kaim, W.; Schwederski, B.; Heilmann, O.; Hornung, F. M. Coordination Compounds of Pteridine, Alloxazine and Flavin Ligands: Structures and Properties. *Coord. Chem. Rev.* **1999**, *182* (1), 323–342.
- (9) Alonso-De Castro, S.; Ruggiero, E.; Ruiz-De-Angulo, A.; Rezabal, E.; Mareque-Rivas, J. C.; Lopez, X.; López-Gallego, F.; Salassa, L. Riboflavin as a Bioorthogonal Photocatalyst for the Activation of a Pt^{IV} Prodrug. *Chem. Sci.* **2017**, 8 (6), 4619–4625.
- (10) Alonso-de Castro, S.; Terenzi, A.; Hager, S.; Englinger, B.; Faraone, A.; Martínez, J. C.; Galanski, M.; Keppler, B. K.; Berger, W.; Salassa, L. Biological Activity of Pt^{IV} Prodrugs Triggered by Riboflavin-Mediated Bioorthogonal Photocatalysis. *Sci. Rep.* **2018**, 8 (1), No. 17198.
- (11) Gurruchaga-Pereda, J.; Martínez-Martínez, V.; Rezabal, E.; Lopez, X.; Garino, C.; Mancin, F.; Cortajarena, A. L.; Salassa, L. Flavin Bioorthogonal Photocatalysis Toward Platinum Substrates. *ACS Catal.* **2020**, *10* (1), 187–196.
- (12) Mazzei, L. F.; Martínez, Á.; Trevisan, L.; Rosa-Gastaldo, D.; Cortajarena, A. L.; Mancin, F.; Salassa, L. Toward Supramolecular Nanozymes for the Photocatalytic Activation of Pt(IV) Anticancer Prodrugs. *Chem. Commun.* **2020**, *56* (72), 10461–10464.
- (13) Velasco-Lozano, S.; Castro, S. A.; Sanchez-Cano, C.; Benítez-Mateos, A. I.; López-Gallego, F.; Salassa, L. Metal Substrate Catalysis in the Confined Space for Platinum Drug Delivery. *Chem. Sci.* **2022**, 13 (1), 59–67.
- (14) Sánchez-Camacho, J.; Infante-Tadeo, S.; Carrasco, A. C.; Scoditti, S.; Martínez, Á.; Barroso-Bujans, F.; Sicilia, E.; Pizarro, A. M.; Salassa, L. Flavin-Conjugated Pt(IV) Anticancer Agents. *Inorg. Chem.* **2023**, *62* (14), 5644–5651.
- (15) Chilamari, M.; Immel, J. R.; Chen, P.-H.; Alghafli, B. M.; Bloom, S. Flavin Metallaphotoredox Catalysis: Synergistic Synthesis in Water. *ACS Catal.* **2022**, *12* (7), 4175–4181.
- (16) Lin, K.; Gómez-Bombarelli, R.; Beh, E. S.; Tong, L.; Chen, Q.; Valle, A.; Aspuru-Guzik, A.; Aziz, M. J.; Gordon, R. G. A Redox-Flow Battery with an Alloxazine-Based Organic Electrolyte. *Nat. Energy* **2016**, *1* (9), No. 16102.
- (17) Morán Plata, M. J.; Marretta, L.; Gaztelumendi, L.; Pieslinger, G. E.; Carballo, R. R.; Rezabal, E.; Barone, G.; Martínez-Martínez, V.; Terenzi, A.; Salassa, L. Alloxazine-Based Ligands And Their Ruthenium Complexes As NADH Oxidation Catalysts And G4 Binders. *ChemRxiv* 2024, No. 1, DOI: 10.26434/chemrxiv-2024-08dkm.

- (18) Gill, M. R.; Thomas, J. A. Ruthenium(II) Polypyridyl Complexes and DNA—from Structural Probes to Cellular Imaging and Therapeutics. *Chem. Soc. Rev.* **2012**, *41* (8), 3179–3192.
- (19) Dalton, S. R.; Glazier, S.; Leung, B.; Win, S.; Megatulski, C.; Burgmayer, S. J. N. DNA Binding by Ru(II)—Bis(Bipyridine)—Pteridinyl Complexes. *JBIC, J. Biol. Inorg. Chem.* **2008**, *13* (7), 1133—1148.
- (20) Olaprath, W.; McGuire, M. E. Comparison of the Electrochemical Reductions of Ru(II) Complexes of Dipyrido[3,2-a:2',3'-c]Phenazine and 10,12-Dimethylpteridino[6,7-f][1,10]-Phenanthroline-11,13(10H,12H)-Dione (an Alloxazine Analog) in Aprotic and Mixed Aprotic/Aqueous Media. *Inorg. Chim. Acta* 2012, 383, 312–315.
- (21) Gao, F.; Chao, H.; Zhou, F.; Yuan, Y.-X.; Peng, B.; Ji, L.-N. DNA Interactions of a Functionalized Ruthenium(II) Mixed-Polypyridyl Complex [Ru(bpy)₂ppd]²⁺. *J. Inorg. Biochem.* **2006**, 100 (9), 1487–1494.
- (22) Tang, W.; Zhu, Z.; Tan, L. [Ru(bpy)₂(7-CH₃-dppz)]²⁺ and [Ru(phen)₂(7-CH₃-dppz)]²⁺ as Metallointercalators That Affect Third-Strand Stabilization of the Poly(U)poly(A)*poly(U) Triplex. *Mol. BioSyst.* **2016**, *12* (5), 1478–1485.
- (23) Mataranga-Popa, L. N.; Torje, I.; Ghosh, T.; Leitl, M. J.; Späth, A.; Novianti, M. L.; Webster, R. D.; König, B. Synthesis and Electronic Properties of π -Extended Flavins. *Org. Biomol. Chem.* **2015**, 13 (40), 10198–10204.
- (24) Castillo, J.; Orrego Hernández, J.; Portilla, J. Cs₂CO₃-Promoted Direct N-Alkylation: Highly Chemoselective Synthesis of N-Alkylated Benzylamines and Anilines. *Eur. J. Org. Chem.* **2016**, 2016, 3824–3835.
- (25) Tönnemann, J.; Risse, J.; Grote, Z.; Scopelliti, R.; Severin, K. Efficient and Rapid Synthesis of Chlorido-Bridged Half-Sandwich Complexes of Ruthenium, Rhodium, and Iridium by Microwave Heating. Eur. J. Inorg. Chem. 2013, 2013 (26), 4558–4562.
- (26) Ruiz, G. T.; Juliarena, M. P.; Lezna, R. O.; Feliz, M. R.; Ferraudi, G. On the Parallel Formation of Long-Lived Excited States of Dipyridil[3,2-a:2'3'-c]Phenazine, Dppz: A Contrast between the Electrochemically and Photochemically Induced Reduction of Dppz. *J. Photochem. Photobiol., A* **2006**, 179 (3), 289–297.
- (27) Schäfer, B.; Görls, H.; Presselt, M.; Schmitt, M.; Popp, J.; Henry, W.; Vos, J. G.; Rau, S. Derivatives of Dipyrido[3,2-a:2',3'-c]Phenazine and Its Ruthenium Complexes, Influence of Arylic Substitution on Photophysical Properties. *Dalton Trans.* **2006**, *18*, 2225–2231.
- (28) McKinley, A. W.; Lincoln, P.; Tuite, E. M. Environmental Effects on the Photophysics of Transition Metal Complexes with Dipyrido[2,3-a:3',2'-c]Phenazine (Dppz) and Related Ligands. *Coord. Chem. Rev.* **2011**, 255 (21), 2676–2692.
- (29) Betanzos-Lara, S.; Salassa, L.; Habtemariam, A.; Novakova, O.; Pizarro, A. M.; Clarkson, G. J.; Liskova, B.; Brabec, V.; Sadler, P. J. Photoactivatable Organometallic Pyridyl Ruthenium(II) Arene Complexes. *Organometallics* **2012**, *31* (9), 3466–3479.
- (30) Mal, M., Mandal, D. Phototautomerism of Alloxazine in Acetic Acid Water Solvent Systems. *J. Mol. Liq.* **2021**, 322, No. 114928.
- (31) Prukała, D.; Sikorska, E.; Koput, J.; Khmelinskii, I.; Karolczak, J.; Gierszewski, M.; Sikorski, M. Acid-Base Equilibriums of Lumichrome and Its 1-Methyl, 3-Methyl, and 1,3-Dimethyl Derivatives. *J. Phys. Chem. A* **2012**, *116* (28), 7474–7490.
- (32) Fees, J.; Kaim, W.; Moscherosch, M.; Matheis, W.; Klima, J.; Krejcik, M.; Zalis, S. Electronic Structure of the "Molecular Light Switch" Bis(Bipyridine)Dipyrido[3,2-a:2′,3′-c]Phenazineruthenium-(2+). Cyclic Voltammetric, UV/Visible and EPR/ENDOR Study of Multiply Reduced Complexes and Ligands. *Inorg. Chem.* 1993, 32 (2), 166–174.
- (33) Robins, K.; Osorio-Lozada, A. Exploiting Duality in Nature: Industrial Examples of Enzymatic Oxidation and Reduction Reactions. *Catal. Sci. Technol.* **2012**, *2* (8), 1524–1530.
- (34) Tensi, L.; Macchioni, A. Extremely Fast NADH-Regeneration Using Phosphonic Acid as Hydride Source and Iridium-Pyridine-2-Sulfonamidate Catalysts. *ACS Catal.* **2020**, *10* (14), 7945–7949.

- (35) Bhoyar, T.; Kim, D. J.; Abraham, B. M.; Gupta, A.; Maile, N.; Manwar, N. R.; Tonda, S.; Vidyasagar, D.; Umare, S. S. Accelerating NADH Oxidation and Hydrogen Production with Mid-Gap States of Nitrogen-Rich Carbon Nitride Photocatalyst. *iScience* **2022**, 25 (12), No. 105567.
- (36) Bucci, A.; Dunn, S.; Bellachioma, G.; Menendez Rodriguez, G.; Zuccaccia, C.; Nervi, C.; Macchioni, A. A Single Organoiridium Complex Generating Highly Active Catalysts for Both Water Oxidation and NAD+/NADH Transformations. ACS Catal. 2017, 7 (11), 7788–7796.
- (37) Fan, Z.; Huang, J.; Huang, H.; Banerjee, S. Metal-Based Catalytic Drug Development for Next-Generation Cancer Therapy. *ChemMedChem* **2021**, *16* (16), 2480–2486.
- (38) Betanzos-Lara, S.; Liu, Z.; Habtemariam, A.; Pizarro, A. M.; Qamar, B.; Sadler, P. J. Organometallic Ruthenium and Iridium Transfer-Hydrogenation Catalysts Using Coenzyme NADH as a Cofactor. *Angew. Chem., Int. Ed.* **2012**, *51* (16), 3897–3900.
- (39) Huang, H.; Banerjee, S.; Qiu, K.; Zhang, P.; Blacque, O.; Malcomson, T.; Paterson, M. J.; Clarkson, G. J.; Staniforth, M.; Stavros, V. G.; et al. Targeted Photoredox Catalysis in Cancer Cells. *Nat. Chem.* **2019**, *11* (11), 1041–1048.
- (40) Mengele, A. K.; Weixler, D.; Chettri, A.; Maurer, M.; Huber, F. L.; Seibold, G. M.; Dietzek, B.; Eikmanns, B. J.; Rau, S. Switching the Mechanism of NADH Photooxidation by Supramolecular Interactions. *Chem. Eur. J.* **2021**, *27* (68), 16840–16845.
- (41) Scoditti, S.; Dabbish, E.; Pieslinger, G. E.; Rezabal, E.; Lopez, X.; Sicilia, E.; Salassa, L. Flavin-Mediated Photoactivation of Pt(IV) Anticancer Complexes: Computational Insights on the Catalytic Mechanism. *Phys. Chem. Chem. Phys.* **2022**, 24 (9), 5323–5329.
- (42) Zhang, Q.; Khetan, A.; Er, S. A Quantitative Evaluation of Computational Methods to Accelerate the Study of Alloxazine-Derived Electroactive Compounds for Energy Storage. *Sci. Rep.* **2021**, *11* (1), No. 4089.
- (43) Streciwilk, W.; Terenzi, A.; Misgeld, R.; Frias, C.; Jones, P. G.; Prokop, A.; Keppler, B. K.; Ott, I. Metal NHC Complexes with Naphthalimide Ligands as DNA-Interacting Antiproliferative Agents. *ChemMedChem* **2017**, *12* (3), 214–225.
- (44) Hager, L. A.; Mokesch, S.; Kieler, C.; Alonso-de Castro, S.; Baier, D.; Roller, A.; Kandioller, W.; Keppler, B. K.; Berger, W.; Salassa, L.; Terenzi, A. Ruthenium—Arene Complexes Bearing Naphthyl-Substituted 1,3-Dioxoindan-2-Carboxamides Ligands for G-Quadruplex DNA Recognition. *Dalton Trans.* **2019**, 48 (32), 12040—12049.
- (45) Hartshorn, R. M.; Barton, J. K. Novel Dipyridophenazine Complexes of Ruthenium(II): Exploring Luminescent Reporters of DNA. J. Am. Chem. Soc. 1992, 114 (15), 5919–5925.
- (46) Friedman, A. E.; Chambron, J. C.; Sauvage, J. P.; Turro, N. J.; Barton, J. K. A Molecular Light Switch for DNA: Ru(bpy)₂(dppz)²⁺. *J. Am. Chem. Soc.* **1990**, *112* (12), 4960–4962.
- (47) McQuaid, K.; Abell, H.; Gurung, S. P.; Allan, D. R.; Winter, G.; Sorensen, T.; Cardin, D. J.; Brazier, J. A.; Cardin, C. J.; Hall, J. P. Structural Studies Reveal Enantiospecific Recognition of a DNA G-Quadruplex by a Ruthenium Polypyridyl Complex. *Angew. Chem., Int. Ed.* **2019**, *58* (29), 9881–9885.
- (48) McQuaid, K.; Hall, J. P.; Baumgaertner, L.; Cardin, D. J.; Cardin, C. J. Three Thymine/Adenine Binding Modes of the Ruthenium Complex Λ-[Ru(TAP)₂(dppz)]²⁺ to the G-Quadruplex Forming Sequence d(TAGGGTT) Shown by X-Ray Crystallography. *Chem. Commun.* **2019**, 55 (62), 9116–9119.
- (49) Figueiredo, J.; Mergny, J.-L.; Cruz, C. G-Quadruplex Ligands in Cancer Therapy: Progress, Challenges, and Clinical Perspectives. *Life Sci.* **2024**, 340, No. 122481.
- (50) Ducani, C.; Bernardinelli, G.; Högberg, B.; Keppler, B. K.; Terenzi, A. Interplay of Three G-Quadruplex Units in the KIT Promoter. *I. Am. Chem. Soc.* **2019**. *141* (26). 10205–10213.
- (51) Bignon, E.; Spinello, A.; Miclot, T.; D'Anna, L.; Ducani, C.; Grandemange, S.; Barone, G.; Monari, A.; Terenzi, A. Predicting the Three-Dimensional Structure of the c-KIT Proto-Oncogene Promoter

- and the Dynamics of Its Strongly Coupled Guanine Quadruplexes. J. Phys. Chem. Lett. 2023, 14 (20), 4704–4710.
- (52) Terenzi, A.; Bonsignore, R.; Spinello, A.; Gentile, C.; Martorana, A.; Ducani, C.; Högberg, B.; Almerico, A. M.; Lauria, A.; Barone, G. Selective G-Quadruplex Stabilizers: Schiff-Base Metal Complexes with Anticancer Activity. *RSC Adv.* **2014**, *4* (63), 33245–33256.
- (53) Cullen, A. A.; Long, C.; Pryce, M. T. Explaining the Role of Water in the "Light-Switch" Probe for DNA Intercalation: Modelling Water Loss from [Ru(phen)₂(dppz)]²⁺•2H₂O Using DFT and TD-DFT Methods. *J. Photochem. Photobiol., A* **2021**, *410*, No. 113169.
- (54) Frisch, M. J.; Trucks, G. W.; Schlegel, H. B.; Scuseria, G. E.; Robb, M. A.; Cheeseman, J. R.; Scalmani, G.; Barone, V.; Petersson, G. A.; Nakatsuji, H. et al. *Gaussian 16*, revision C.02; Gaussian, Inc.: Wallingford, 2019.
- (55) Grimme, S.; Ehrlich, S.; Goerigk, L. Effect of the Damping Function in Dispersion Corrected Density Functional Theory. *J. Comput. Chem.* **2011**, 32 (7), 1456–1465.
- (56) Szabo, A.; Ostlund, N. S. Modern Quantum Chemistry: Introduction to Advanced Electronic Structure Theory; McGraw-Hill: New York, 1996.
- (57) Borfecchia, E.; Garino, C.; Salassa, L.; Ruiu, T.; Gianolio, D.; Zhang, X.; Attenkofer, K.; Chen, L. X.; Gobetto, R.; Sadler, P. J.; Lamberti, C. X-Ray Transient Absorption Structural Characterization of the ³MLCT Triplet Excited State of Cis-[Ru(bpy)₂(py)₂]²⁺. *Dalton Trans.* **2013**, 42 (18), 6564–6571.
- (58) Pieslinger, G. E.; Cadranel, A.; Baraldo, L. M. Where's the Spin? A DFT Study of Mixed-Valence Cyanide-Bridged Ruthenium Polypyridines. *J. Braz. Chem. Soc.* **2020**, *31* (11), 2360–2370.
- (59) Weigend, F.; Ahlrichs, R. Balanced Basis Sets of Split Valence, Triple Zeta Valence and Quadruple Zeta Valence Quality for H to Rn: Design and Assessment of Accuracy. *Phys. Chem. Chem. Phys.* **2005**, 7 (18), 3297–3305.
- (60) Andrae, D.; Häußermann, U.; Dolg, M.; Stoll, H.; Preuß, H. Energy-Adjustedab Initio Pseudopotentials for the Second and Third Row Transition Elements. *Theor. Chim. Acta* **1990**, *77* (2), 123–141.
- (61) Scalmani, G.; Frisch, M. J. Continuous Surface Charge Polarizable Continuum Models of Solvation. I. General Formalism. *J. Chem. Phys.* **2010**, *132* (11), No. 114110.
- (62) Tomasi, J.; Mennucci, B.; Cammi, R. Quantum Mechanical Continuum Solvation Models. Chem. Rev. 2005, 105 (8), 2999–3094.
- (63) Miertuš, S.; Scrocco, E.; Tomasi, J. Electrostatic Interaction of a Solute with a Continuum. A Direct Utilizaion of AB Initio Molecular Potentials for the Prevision of Solvent Effects. *Chem. Phys.* **1981**, *55* (1), 117–129.
- (64) Schlegel, H. B. Optimization of Equilibrium Geometries and Transition Structures. *J. Comput. Chem.* **1982**, 3 (2), 214–218.
- (65) Petit, L.; Maldivi, P.; Adamo, C. Predictions of Optical Excitations in Transition-Metal Complexes with Time Dependent-Density Functional Theory: Influence of Basis Sets. *J. Chem. Theory Comput.* **2005**, *1* (5), 953–962.
- (66) Stratmann, R. E.; Scuseria, G. E.; Frisch, M. J. An Efficient Implementation of Time-Dependent Density-Functional Theory for the Calculation of Excitation Energies of Large Molecules. *J. Chem. Phys.* 1998, 109 (19), 8218–8224.
- (67) O'Boyle, N. M.; Tenderholt, A. L.; Langner, K. M. Cclib: A Library for Package-Independent Computational Chemistry Algorithms. *J. Comput. Chem.* **2008**, 29 (5), 839–845.
- (68) Dennington, R.; Keith, T.; Millam, J. GaussView, version 5; Semichem Inc.: Shawnee Mission, KS, 2009.
- (69) Brynn Hibbert, D.; Thordarson, P. The Death of the Job Plot, Transparency, Open Science and Online Tools, Uncertainty Estimation Methods and Other Developments in Supramolecular Chemistry Data Analysis. *Chem. Commun.* **2016**, 52 (87), 12792–12805.
- (70) Dolomanov, O. V.; Bourhis, L. J.; Gildea, R. J.; Howard, J. A. K.; Puschmann, H. OLEX2: A Complete Structure Solution, Refinement and Analysis Program. *J. Appl. Crystallogr.* **2009**, 42 (2), 339–341.

- (71) Sheldrick, G. M. SHELXT Integrated Space-Group and Crystal-Structure Determination. *Acta Crystallogr., Sect. A: Found. Adv.* **2015**, *71* (1), 3–8.
- (72) Sheldrick, G. M. Crystal Structure Refinement with SHELXL. *Acta Crystallogr.* **2015**, *C71* (1), 3–8.